Electronic Materials Letters
https://doi.org/10.1007/s13391-023-00481-w

ORIGINAL ARTICLE - ELECTRONICS, MAGNETICS AND PHOTONICS

Forming-Free and Non-linear Resistive Switching in Bilayer HfO_x/TaO_x Memory Devices by Interface-Induced Internal Resistance

Mari Napari[1,2] · Spyros Stathopoulos[1,3] · Themis Prodromakis[3] · Firman Simanjuntak[1]

Received: 18 May 2023 / Accepted: 25 December 2023

Abstract

Resistive switching memory devices with tantalum oxide (TaO_x) and hafnium oxide (HfO_x) mono- and bilayers were fabricated using atomic layer deposition. The bilayer devices with Ti and TiN electrodes show non-linear switching characteristics, and can operate without requiring an initial electroforming step. The insertion of the HfO_x layer induces the switching behaviour on single layer TaO_x that shows Zener diode-like characteristics, with conductivity depending on the top electrode metal. The electronic conductivity mechanism study shows Schottky emission at low voltage regime followed by tunneling at higher applied bias, both indicating interface-dominated conduction. The switching mechanism study is supported by X-ray photoelectron spectroscopy characterization of the films that show a formation of TaO_xN_y and TaN_x species at the oxide-electrode interface. This interfacial layer serves as a high resistivity barrier layer enabling the homogeneous resistive switching behavior.

Graphical Abstract

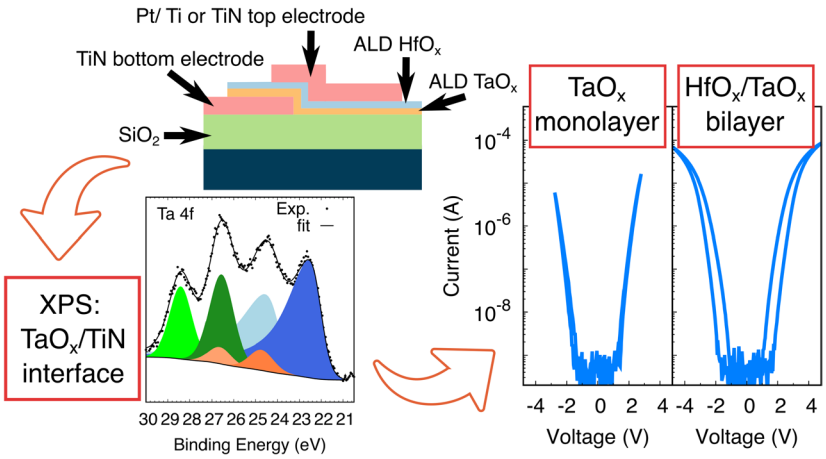

Keywords Resistive switching · Memory devices · Oxides · Atomic layer deposition

✉ Firman Simanjuntak
f.m.simanjuntak@soton.ac.uk

Mari Napari
mari.napari@kcl.ac.uk

[1] School of Electronics and Computer Science, University of Southampton, Southampton SO17 1BJ, UK

[2] Present Address: Department of Physics, King's College London, Strand, London WC2R 2LS, UK

[3] School of Engineering, University of Edinburgh, Edinburgh EH9 3JL, UK

Published online: 06 February 2024

1 Introduction

Resistive random access memory (RRAM) is considered to be the most promising candidate to replace the NAND flash memory when its scaling ends [1]. The advantages of the RRAM include its simple structure, feasibility for high-density 3D applications, and low-power consumption [2]. However, the remaining challenges, such as the need for a high-voltage electroforming and current sneak-path issues in the array have hindered the commercialization of the RRAM technology [2, 3]. Electroforming-free RRAM are particularly necessary when considering the low-voltage supplies supported by more advanced CMOS technology nodes [4]. Meanwhile, in order to avoid the sneak-path issues in the array configuration, the RRAM cell is usually stacked with a selector (either diode or transistor) to produce non-linear $I-V$ behavior [5].

Employing a bilayer stack in the resistive switching memory cell can overcome some of the RRAM issues by reducing the forming voltages, and improving the switching stability and uniformity [6]. Bilayer systems can also stabilize the multi-bit operation in the analog resistive switching performance, which is a critical factor for the high-capacity memory applications [7], as well as in the adaptation of these devices in neuromorphic computing [8].

TaO_x and HfO_x bilayers for resistive switching have demonstrated to have forming-free and self-rectifying characteristics when combined with noble metal electrodes such as Pt [9–15]. However, there seems to be discrepancies in the reported device operation, i.e. whether the resistive switching takes place in the TaO_x [12, 13], or HfO_x layer [9, 11], and it is clear that the oxide deposition methods, layer thicknesses, electrode materials, and oxide-metal and oxide-oxide interfaces all play significant roles in the device operation and performance. For instance, in the reports on TaO_x & HfO_x bilayer memory devices either one, typically TaO_x [13–15], or both [10] oxide layers are fabricated using physical vapor deposition (PVD) methods, namely magnetron/RF sputtering. PVD provides better tuneability on the stoichiometry and vacancy concentration via the control of the oxygen partial pressure during the deposition, and in these devices the resistive switching can be attributed to the formation of the conductive filament in the thicker (> 10 nm) TaO_x layer [13]. In devices where both of the layers are fabricated by chemical approaches such as atomic layer deposition (ALD), e.g. Refs [9, 11], with the HfO_x grown first on the bottom electrode in Pt/TaO_x/HfO_x/TiN stacks, the interfaces between the subsequently deposited layers appear critical: e.g. by chemical modification leading to increased number of deep trap states within the film that enable the resistive switching, or by forming Schottky barriers to constitute the rectifying behaviour [9, 11].

In this paper we propose that the electroforming-free and the non-linear behavior can be achieved by a (HfO_x/TaO_x) bilayer RRAM design without the necessity of a selector stack. Tuneable non-linearity capability of a single RRAM cell is a highly desirable feature as it can ideally be utilized in fabrication of small footprint crossbar arrays as the non-linearity could eliminate the need for external selector devices [16, 17]. Atomic layer deposited (ALD) Ta and Hf oxides were chosen as they have already shown compatibility with existing technologies and back-end-of-line (BEOL) processes for monolithic 3D integration [18, 19]. The use of ALD also enables the fabrication of uniform and pinhole-free films, allowing the use of ultra-thin films in the resistive switching devices also in vertical geometries, and thus the miniaturization of memory components to match the advanced technology nodes.

2 Methods

The patterning of device structures were done on 150 mm Si wafers with 200 nm thermal oxide. A photolithography process with negative photoresist (AZ2070, MicroChemicals GmbH) was used for the lift-off patterning of bottom electrodes: room-temperature sputtered (Angstrom Engineering) 50 nm TiN with 10 nm Ti adhesion layer between the TiN and SiO_2. A Ti target was used in the TiN reactive sputtering with nitrogen plasma (20 sccm, 10 mTorr, 600 W). The TaO_x layer (5 nm) was deposited by plasma-enhanced atomic layer deposition (ALD) (Oxford Instruments FlexAL, with 13.56 MHz remote inductively-coupled plasma source) using pentakis(dimethylamino) tantalum (PDMAT, $Ta(N(CH_3)_2)_5$ from Pegasus Chemicals) precursor with O_2-plasma as the oxygen source. The PDMAT source was kept at 65 °C and the TaO_x deposition temperature was 200 °C. One ALD cycle consisted of 1.25 s PDMAT pulse/8 s purge/4 s O_2-plasma pulse (250 W, 50 sccm O_2 flow)/3 s purge. This process yielded a growth per cycle (GPC) of 0.93 Å on SiO_2/Si substrate, measured by a spectroscopic ellipsometer (J A Woollam M-2000). Subsequently, the wafer was transferred to another ALD reactor (Veeco Savannah S200) where the HfO_x (3 nm), was grown by thermal ALD process at 175 °C using tetrakis(dimethylamino)hafnium (TDMAH, $Hf(N(CH_3)_2)_4$ from Sigma-Aldrich), sublimed at 75 °C, and H_2O. Each HfO_x ALD cycle consisted of 0.2 s TDMAH pulse/10 s purge/0.03 s H_2O pulse/10 s purge. Prior to the TDMAH pulse Ar was released in the precursor container for 0.05 s via a boost valve to enable enhanced precursor delivery to the deposition chamber. The HfO_2 GPC on SiO_2 /Si substrate was 1.05 Å. A positive photoresist (Microposit S1813) was used as an etching mask for oxide patterning by ion beam etching (Oxford Instruments Ionfab 300,

800 W Ar beam) prior to deposition of top electrodes (TE). 60 nm TiN or 10 nm Ti + 15 nm Pt top electrodes were fabricated similarly to the bottom electrodes, using negative photoresist lift-off process and magnetron sputtering at room temperature. In the Pt/Ti top electrode stacks the Pt served as an oxidation barrier to prevent the formation of insulating TiO_2 layer on the electrode surface. The electrode materials were selected because they are typical semiconductor processing materials, Ti is commonly used for metal interconnects and TiN in diffusion barriers. The device structure and layout are presented in Fig. 1a. For materials characterization, single TaO_x and HfO_x films on on SiO_2/Si, and unpatterned TE/HfO_x/TaO_x/TiN samples were prepared. For XPS depth profiling the TiN top electrode thickness was reduced from 60 to 20 nm.

Atomic force microscopy (AFM, Bruker Icon) in peak force mode was used to investigate the topographic properties of the thin film stacks. X-ray photoelectron spectroscopy (XPS, ThermoFisher ThetaProbe with Al K_α 1.487 eV X-ray source, beam spot diameter 400 µm) was used to characterize the oxide films and to depth profile the device stacks. For depth profiling Ar^+ ion etching was applied (1 kV, 1 µA, raster area 2 mm × 2 mm) and core level spectra of relevant elements were collected after each 30 s etch step. Ar^+ beam etch with lower energy (0.5 keV) was used for surface cleaning before measuring the oxide film samples. The XPS data was analysed using CasaXPS analysis software, shirley background was used in the peak deconvolution together with Gaussian-Lorentzian GL(30) lineshape, except for metallic and nitride peaks, where an asymmetric lineshape was used. The devices were measured using a Cascade probe station and ArC One measurement platform. During the measurement the positive and negative bias voltages were applied to the top electrode while the bottom electrode was kept grounded.

3 Results and Discussion

3.1 Preliminary Materials Characterization

Prior to the device fabrication, the growth and physical properties of the ALD oxide films were investigated. The XPS analysis of 10 nm oxide films grown on SiO_2/Si substrates confirmed that the used ALD processes yielded nearly stoichiometric HfO_2 and Ta_2O_5 films, with very minor sub-oxide concentration detected in the tantalum oxide film, presented in Fig. 1b, c respectively. The excess oxygen can be associated with the hydrogen-containing species, namely -OH and physisorbed water, as shown in the Supporting Information Figs. S1 and S2. In the Ta_2O_5 film a minor carbon content ($\leq 1\%$) was also measured, but no other impurities were detected. The sub-oxides and impurities were also shown as a slight increase in the gap states ca. 1.4 eV below the Fermi level in the valence band edge spectrum of the TaO_x sample, seen in Fig. S2d. Atomic force microscopy scans confirmed that each of the subsequently deposited layer (bottom TiN, TaO_x, and HfO_x) is uniform and smooth, with RMS roughness of the HfO_x/TaO_x/TiN film stack being $r_{RMS} \approx 0.2$ nm (Fig. 1d). The AFM images of the TiN bottom electrode and TaO_x/TiN layers are presented in Fig. S3.

3.2 Device Characterization

Monolayers: No resistive switching was observed in monolayer HfO_x and TaO_x devices, as depicted in Figs. 2a(i–iv). Both the TE/HfO_x/TiN devices [Fig. 1a(i, ii)] exhibit pure ohmic conduction, as confirmed by the linear I-V behaviour (Fig. S4). The low resistance ($R \approx 10$ kΩ) of the HfO_x, even at higher film thickness up to 7 nm, is likely a result of the relatively low deposition temperature (175 °C), which leads to a lower film density and increases contents of light

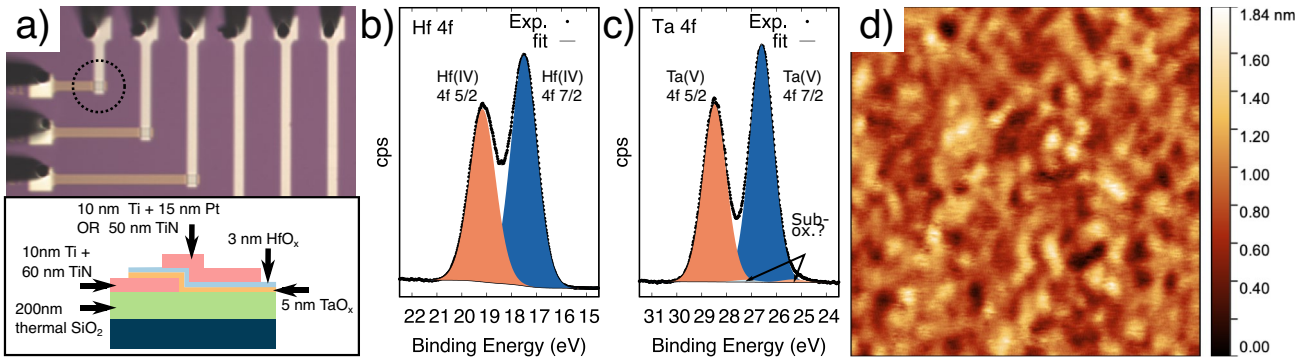

Fig. 1 **a** Top: an example of the cross-point device layout, the dark features on the top and left of the image are the attached probes of the probecard measurement setup; bottom: a schematic of the device structure. **b** XPS Hf 4f spectrum of HfO_x film and **c** XPS Ta4f spectrum of TaO_x film, both deposited on SiO_2/Si. **d** Atomic force micrograph of 3 nm HfO_x/5 nm TaO_x/50 nm TiN thin film stack

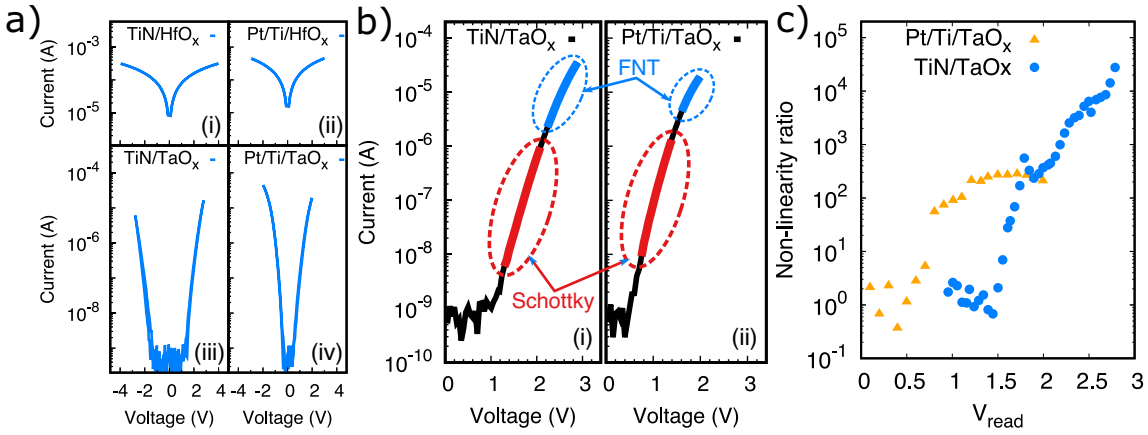

Fig. 2 **a** $I-V$ characteristics of a monolayer HfO_x (7 nm) devices with (*i*) TiN and (*ii*) Pt/Ti top electrode; and a monolayer TaO_x (5 nm) devices with (*iii*) TiN and (*iv*) Pt/Ti top electrode. All the devices have TiN bottom electrodes. **b** $I-V$ curves of the TaO_x monolayer devices with *i* TiN and *ii* Pt/Ti top electrodes, respectively, showing the regions where the Schottky emission (red) and Fowler–Nordheim tunneling (FNT, blue) dominate the electronic conduction. **c** Non-linearity ratio $I(V_{read})/I(\frac{1}{2}V_{read})$ of the TaO_x monolayer devices with TiN (blue circles) and Pt/Ti (orange triangles) top electrodes, respectively. All the data in **a**–**c** are measured from pristine devices with 5×5 µm device area. (Color figure online)

element impurities, such as hydrogen and carbon, that can have a detrimental impact on the electrical characteristics [20, 21]. As discussed earlier, in our HfO_x films the carbon content was below the detection level of our XPS system (< 1 at%), but it was observed that the films contained ca. 10 % of excess, non Hf-bound oxygen in the form of hydrogen containing species i.e. hydroxyl OH– and physisorbed H_2O residues from the TDMAH + H_2O deposition process which can cause the observed high leakage current as high-mobility interstitials [22]. Hydrogen and hydrogen containing species can also hamper the formation and migration of the oxygen vacancies required for the resistive switching [23, 24], as well as accumulate into electron traps at the oxide-electrode interface [25].

Like the HfO_x, the TaO_x monolayer devices exhibit no resistive switching behaviour, as shown in Fig. 2a(iii–iv). Instead, the TaO_x devices show Zener diode (varistor) characteristics, where the current below threshold voltage, approximately 1.5 V for TiN TE, and 0.5 V for Pt/Ti TE devices, respectively, is very low (0.1 nA regime), and increases rapidly above the threshold. The conduction mechanism analysis shows that the electron conduction is dominated by Schottky emission at the low-voltage range above the threshold voltage, and at higher voltages the Fowler–Nordheim tunneling becomes the dominant mechanism, as shown in Fig. 2b. The $(\log(I) \propto \sqrt{V})$ and $(\log(I/V^2) \propto I/V)$ fits for defining the Schottky emission and the Fowler–Nordheim tunneling (FNT) regimes, respectively, are shown in Fig. S5. These results indicate that significant barrier height exists at the TaO_x/TiN junctions. In addition, the non-linearity ratio $I(V_{read})/I(\frac{1}{2}V_{read})$ of the TiN/TaO_xdevice can achieve up to 2.7×10^4 when 2.8 V is applied. The Pt/Ti/TaO_x device also exhibit a non-linear behaviour, but with a more modest non-linearity ratio of $\sim$ 200 at 1.5 V V_{read} (Fig. 2c).

The Schottky emission and Fowler–Nordheim tunneling are well known electron transfer mechanisms in oxide thin film systems [26], including the TaO_x thin film diodes, where the dominant mechanisms are largely determined by the work function of the biased electrode [27]. Moreover TiN has a high metallic stability, and the oxidation of this film for TiON interfacial layer formation is a diffusion-limited process which doesn't readily occur at room temperature [28]. Ti has more negative Gibbs free energy of TiO_x formation ($\Delta G^0 = -889.5$ kJ/mol) [29] than that of TiN forming TiON ($\Delta G^0 = -580.3$ kJ/mol) [28] which leads to more efficient oxygen scavenging from the oxide layer. When we replace the TiN top electrode with Ti, we can assume that a TiO_x layer forms at the interface. This TiO_x interfacial layer decreases the barrier height at the electrode/oxide interface via several different mechanisms e.g. change in the electron affinity of the formed oxide and formation of metal-induced gap states and positively charged defects [30], and hence, decreases the non-linearity of the Pt/Ti/TaO_x device.

Bilayers: the insertion of the thin (3 nm) HfO_x into the TE/TaO_x/TiN diode stack induces resistive switching behavior, as shown in Fig. 3a, b. The bilayer devices do not require a forming process to activate the switching characteristics, and they exhibit bipolar switching mode, where positive and negative bias turn On (set) and Off (reset) the device, respectively. The pristine TiN/HfO_x/TaO_x/TiN (TiN/bi-) devices have a high resistance both at high and low resistance states

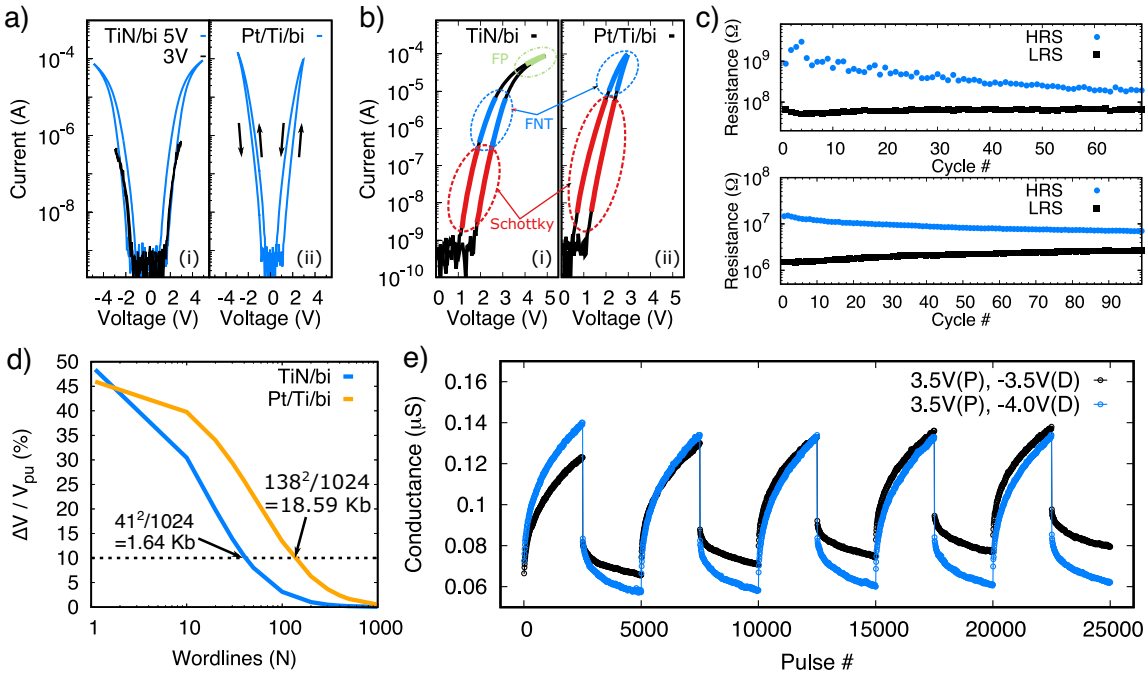

Fig. 3 **a** $I-V$ characteristics of bilayer HfO_x (3 nm)/TaO_x (5 nm) devices with (*i*) TiN and (*ii*) Pt/Ti top electrodes (TE), respectively. **b** Same $I-V$ curves of the bilayer devices with (*i*) TiN and (*ii*) Pt/Ti TE highlighting the regions where the Schottky emission (red), Fowler–Nordheim tunneling (FNT, blue) and Frenkel-Poole emission (FP, green) dominate the electronic conduction. **d** Read margin ($\Delta V/V$) on the crossbar wordline number based on Eq. (1). **e** Endurance plots showing the stabilization of the high and low resistance states (HRS, LRS) of the TiN/bi- (top) and Pt/Ti/bi- (bottom) devices, measured from $I-V$ sweeps at $V_{read} = 1.5$ V. **d** Potentiation(P)/Depression(D) plots of a Pt/Ti/bi- device with pulse scheme amplitudes of 3.5 V (P) & −3.5 V (D) (black) and 3.5 V (P) and −4.0 V (D) (blue), respectively; note that the pulse width is 0.1 ms and $V_{read} = 1.5$ V. (Color figure online)

(HRS, LRS), ca. 1 GΩ at HRS and 65 MΩ at LRS, measured at $V_{read} = 1.5$ V. However, the HRS resistance decreases upon the initial $I-V$ sweeping before stabilising to ca. 200 MΩ, resulting in a switching ratio of 3 (Fig. 3c). The TiN/bi- devices can be swept up to 5 V with both polarities without breakdown. However, a voltage > 3 V is required to induce the switching, as devices swept with lower voltage range retain diode characteristics similar to the TaO_x monolayers (Fig. 3a). The conduction mechanisms in different bias regions are shown in Fig. 3b, with detailed analysis in Fig. S6a–c. The conduction mechanisms at the HRS and LRS are found to be similar to the TiN/TaO_x/TiN diodes with both the Schottky emission and Fowler–Nordheim tunneling present. Although the interfacial barriers are changing during the $I-V$ sweeping due to processes that enable the resistive switching characteristics (redox, trapping/de-trapping, and ionic motions), these results indicate that the interface-limited electronic conduction mechanisms dominate also in the bilayer devices. However, if the bias voltage is further increased, the conduction mechanism switches to Frenkel–Poole emission, ($\log(I/V) \propto \sqrt{V}$), as depicted in Fig. 3b. Unlike Schottky emission and Fowler–Nordheim tunneling that are of interfacial type, the Frenkel–Poole emission at high voltage regime indicates a "soft breakdown" by filament formation, and an electron hopping mechanism which could possibly occur via donor defects in the films. Similar behaviour has been reported also with different material systems exhibiting analog resistive switching operation [31].

As in the case of the TaO_x monolayer device characteristics, the choice of the TE metal has a significant impact on the device performance. Figure 3a(ii), b(ii) show $I-V$ curve of a Pt/Ti/HfO_x/TaO_x/TiN (Pt/Ti/bi-) device. It is found that the device can operate at a lower set and reset voltages (±3 V) compared to the TiN/bi- devices. The endurance sweep resistances measured at $V_{read} = 1.5$ V are 15 MΩ and 1.5 MΩ for HRS and LRS, respectively, and stabilise into 7 MΩ (HRS) and 2.5 MΩ (LRS) after some applied $I-V$ sweeps resulting a switching ratio of 2.8 (Fig. 3c). The LRS and HRS of the bilayer devices are found to be depended on the size of the cell, where the current increases as the device area increases, demonstrated in Fig. S7a with measurements of devices with different cell size. We also found that the retention performance of the HRS and LRS of the bilayer devices tend to decay after 500 s, depicted in Fig. S7b. The size dependency and weak retention are the unique feature of interfacial type homogeneous switching mechanism [32]. However, owing

to the high non-linearity, these devices can be beneficial to various short-term memory applications [33, 34]. The non-linearity ($I_{Vset}/I_{0.5Vset}$) of the Pt/Ti/bi- and TiN/bi-devices is found to be 420 and 318, respectively, indicating an excellent selectivity [35–37]. Moreover, the estimation using the Kirchoff equation suggested in Ref. [38]:

$$\frac{\Delta V}{V_{pu}} = \frac{R_{pu}}{\left[R_{LRS}(V_{read})||\left(\frac{2R_{LRS}(V_{read}/2)}{N-1} + \frac{R_{LRS}(V_{read}/2)}{(N-1)^2}\right)\right] + R_{pu}} - \frac{R_{pu}}{\left[R_{HRS}(V_{read})||\left(\frac{2R_{HRS}(V_{read}/2)}{N-1} + \frac{R_{HRS}(V_{read}/2)}{(N-1)^2}\right)\right] + R_{pu}} \quad (1)$$

where here $R_{pu} = R_{LRS}$ and $V_{read} = 1.5$ V with different number of wordlines (N), gives us an estimation of the potential maximum array size. At 10% read margin 41×41 and 138×138 crossbar configurations result in 1.64 Kb and 18.59 Kb for TiN/bi- and Pt/Ti/bi- devices, respectively, as depicted in Fig. 3d.

The switching characteristics of the bilayer devices implicated a potential to analog/synaptic operation. Synaptic characteristic of Pt/Ti/bi- device is presented in Fig. 3e. One epoch training consists of 5000 pulses [each potentiation (P) and depression (D) scheme consisting of 2500 pulses], measured as sequences of programming (P/D) pulses and read pulses ($V_{read} = 1.5$ V). The result indicates that the potentiation scheme is able to produce good analog behavior with thousands of conduction levels ranging from approx. 0.06 µS (base) to 0.14 µS (peak), without significant noise. On the other hand, an abrupt fall of conductance occurs during the first pulse of the depression scheme. We tried to minimize this abrupt fall by decreasing the amplitude of the depression (V_D); however, V_D lower than −4 V is not sufficient for the base to reach the original conductance level (from the previous epoch) which results in dynamic instability.

3.3 Interface Characterization

In order to better understand the observed device characteristics, we conducted XPS analysis to investigate the stack embedded films and the nature of interfacial layers. Figure 4a–d show the 3D-profiles of the Ti 2p, Hf 4f, Ta 4f, and O 1 s core electron spectra, respectively, measured from the Pt/Ti/bi- (Pt/Ti/HfO_x/TaO_x/TiN) stack (see corresponding data of the TiN/bi- stack in the Fig. S8 in the Supporting Information). The 2D evolution of the Hf 4f and Ta 4f spectra as the function of the etching time are shown in the Figs. S9 and S10.

The Ti oxidation at the Ti/HfO_x electrode/oxide interface is clearly seen in the Ti 2p spectrum in Fig. 4e, where the deconvolution reveals the presence of different TiO_x phases. This also contributes to the corresponding HfO_x spectra depicted in Figs. 4f and S8f, which show increased amount of sub-oxide contribution appearing to lower binding energies (Hf 4f 7/2 at ca. 15.9 eV). The Gibbs free energy of formation of HfO_2 ($\Delta G^0 = -1054$ kJ/mol at 300 K) is more negative than that of TiO_2 or TiON ($\Delta G^0_{TiO_2} = -889.5$ kJ/mol, $\Delta G^0_{TiON} = -580.3$ kJ/mol) [28, 29], however it has been shown that a band offset at metal/HfO_2 interface can lead to a formation of doubly-charged negative oxygen interstitials diffusing into the Ti or TiN interface enabling the oxygen scavenging from the HfO_2 film and formation of the TiO_x or TiN_xO_y interface layer [39].

Even more evident signs of changes in the oxide layer composition at the oxide/metal interface can be seen in the TaO_x spectra in Fig. 4c, g, as well as in the Figs. S8c, g that present the corresponding film in the TiN/bi-stack. the Ta

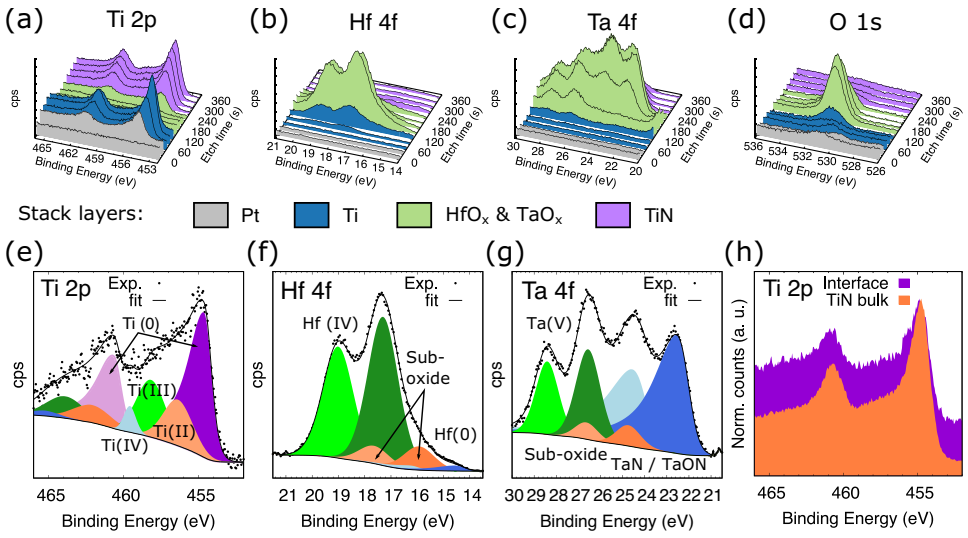

Fig. 4 XPS 3D profiles of the **a** Ti 2p, **b** Hf 4f, **c** Ta 4f, and **d** O 1 s core electrons from a 7 nm Pt/10 nm Ti/3 nm HfO_x /5 nm TaO_x/TiN thin film stack, measured with 30 s Ar^+ ion beam etch steps. **e** Ti 2p spectrum measured at the Ti/HfO_x top electrode interface, **f** Hf 4f spectrum of HfO_x layer, **g** Ta 4f spectrum of the TaO_x layer, and **h** normalised Ti 2p spectrum at the TaO_x/TiN bottom electrode interface compared to the Ti 2p spectrum measured deeper in the TiN film bulk

4f spectra show significant increase in the peak intensities towards lower binding energies when the etching time is increased i.e. the spectrum is measured closer to the TaO_x /TiN interface (see Figs. S9b, S10b). High sub-oxide content is commonly observed in the TaO_x films grown by physical vapor deposition methods for RRAM applications. However, in our film stacks we can assume that the high intensity peaks at 22.8 eV (4f 7/2) and 24.7 eV (4f 5/2) are rather originating from TaN_x and TaO_xN_y species instead of the sub-oxides or metallic Ta. The Ta 4f spectra indicate that at the TiN BE interface majority of the Ta are bound to nitrogen, and the film exhibit the characteristics of a TaO_x only at the HfO_x interface. This is a surprising result considering that a high energy oxygen source (O_2 plasma) was used in the TaO_x deposition by plasma-enhanced ALD. We propose, that during the early stages of the deposition the PDMAT precursor dosing reduces the TiN, and later TaO_x surface [39]. Furthermore, the interface modification of from discrete TaOx/TiN interface to more blended complex with TaN_x, TaO_xN_y and TiO_xN_y species is advanced by the diffusion of oxygen to the TiN layer and the subsequent replacement of oxygen in the growing TaO_x by nitrogen from the TiN electrode surface [40, 41]. Despite using an aminoalkyl precursor in the PEALD, it is unlikely that the nitrogen in the TaO_x layer originates from the PDMAT precursor ligands as no N 1 s signal nor corresponding Ta 4f peaks were detected in the TaO_x films grown in the SiO_2/Si substrates under same conditions.

The XPS results support the $I-V$ characteristics that showed the TaO_x monolayer has higher resistivity compared to the HfO_x (Fig. 2a). This is due to the formation of TaO_xN_y layer at the TaO_x/TiN interface that tend to inhibit the oxygen vacancies formation and movement due to the strong N–O bonds [42]. This interfacial layer provides an internal resistance in the bilayer stack and serves as an electron tunnelling barrier layer [43]. Consequently, the Zener diode characteristic of the TaO_x/TaO_xN_y persists after the insertion of the HfO_x (Fig. 3a). The Ta oxynitride barrier layer dissipates the electrons across the bulk providing a low injection of electrons into the HfO_x layer that facilitates a movement of defects to form low and high resistive regions in the HfO_x layer during set and reset processes, respectively, which leads to the interfacial type homogeneous switching mechanism. Homogeneous switching mechanism relies on a valence change process at the interface region rather than a rupture process of a conducting filament, which tends to exhibit analog performance but with small on/off ratio [32]. This interfacial effect is further enhanced by the formation of TiO_x layer at the interface between the Pt/Ti top electrode and the HfO_x layer; the TiO_x serves as an oxygen reservoir that helps the occurrence of switching at low voltage operation and more stable endurance, which was not observed in devices with TiN top electrodes (Fig. 3b). Note that Pt/Ti/TaO_x/TiN monolayer device is unable to show resistive switching behavior [Fig. 2a(iv)], this could be due to the TiO_x interface being too thin due to the insufficient oxygen scavenging from the TaO_x layer to allow the effective homogeneous mechanism to happen.

According to the $I-V$ measurements, the current injection from Pt/Ti layer to HfO_x layer (Pt/Ti/bi- device) is easier than that of from TaO_x/TiN layer to HfO_x layer, and because of this the switching current of the reverse bias in Pt/Ti TE devices tends to be higher than the forward bias. Similarly, abrupt fall in conductance occurs during the depression process. The abrupt fall indicates that abundant oxygen at the TiO_x top interface layer can be easily ionized and fill large number of oxygen vacancies in the HfO_x layer during the initial depression pulse; however, the initial pulse alone is not sufficient to fill oxygen vacancies near the HfO_x/TaO_x bottom interface region and continuous injection of electrons is required to make the base reach the original conductance (Fig. 3d). Nevertheless, thousands conductance levels with low noise can be produced by potentiation scheme and this performance could be useful for multibit data storage [7] and neuromorphic applications [2].

4 Conclusion

Varistor-like resistive memory devices can be fabricated by stacking a low resistivity film (HfO_x) with a high resistivity film (TaO_x). HfO_x will act as the switching film while TaO_x, and its interface with a TiN electrode serve as an internal resistance in the cell. Neither monolayer devices with an ultra-thin HfO_x nor TaO_x layer alone can perform resistive switching behavior. The low-temperature ALD HfO_x monolayer has high leakage current due to the presence of abundance of OH- species in the film. On the other hand, the TaO_x monolayer on TiN electrode has high resistivity and it exhibits Zener diode characteristics; the formation of TaON at the interface limits the redox reaction in the cell due to the strong N-O bonds, thus, reducing the electron flow into the oxide. The low electron injection into the cell, nevertheless, facilitates redox process at the HfO_x region, inducing a homogeneous non-linear switching in the HfO_x/TaO_x bilayer device. This study provides insight into the fabrication of selector-less resistive memory for realizing high-density arrays.

Supplementary Information The online version contains supplementary material available at https://doi.org/10.1007/s13391-023-00481-w.

Acknowledgements The authors wish to thank the Southampton Nanofabrication Centre cleanroom staff for their help and support and Dr Irwan Purnama from Indonesian National Agency for Research and Innovation for the fruitful discussion on the array level.

Author Contributions MN: Methodology; Writing—original draft; Writing—review and editing. SS: Writing—original draft; Writing—review and editing TP: Funding acquisition; Writing—review and editing. FM: Methodology; Writing—original draft; Writing—review and editing.

Funding This work was financially supported by the European Commission H2020 Grant Agreement No. 824162"A SYnaptically connected Neural Closed-loop Hybrid system (SYNCH)", the United Kingdom Engineering and Physical Sciences Research Council (EPSRC) Programme Grant EP/R024642/1 "Functional Oxide Reconfigurable Technologies (FORTE)", the RAEng Chair in Emerging Technologies (CiET1819/2/93), and European Commission Marie Sklowodska-Curie Action Individual Fellowship Grant Agreement No. 224 (101029535-MENESIS)

Availability of data and materials The data that support the findings of this study are available from the corresponding author upon reasonable request.

Declarations

Conflict of interest The authors have no conflicts to disclose.

References

1. Salahuddin, S., Ni, K., Datta, S.: The era of hyper-scaling in electronics. Nat. Electron. **1**(8), 442–450 (2018). https://doi.org/10.1038/s41928-018-0117-x
2. Zidan, M.A., Strachan, J.P., Lu, W.D.: The future of electronics based on memristive systems. Nat. Electron. **1**(1), 22–29 (2018). https://doi.org/10.1038/s41928-017-0006-8
3. Fang, Z., Yu, H.Y., Li, X., Singh, N., Lo, G.Q., Kwong, D.L.: $HfO_x/TiO_x/HfO_x/TiO_x$ multilayer-based forming-free RRAM devices with excellent uniformity. IEEE Electron Device Lett. **32**(4), 566–568 (2011). https://doi.org/10.1109/LED.2011.2109033
4. Shuai, Y., Ou, X., Luo, W., Mücklich, A., Bürger, D., Zhou, S., Wu, C., Chen, Y., Zhang, W., Helm, M., Mikolajick, T., Schmidt, O.G., Schmidt, H.: Key concepts behind forming-free resistive switching incorporated with rectifying transport properties. Sci. Rep. **3**(1), 2208 (2013). https://doi.org/10.1038/srep02208
5. Zhang, K., Long, S., Liu, Q., Lü, H., Li, Y., Wang, Y., Lian, W., Wang, M., Zhang, S., Liu, M.: Progress in rectifying-based RRAM passive crossbar array. Sci. China Technol. Sci. **54**(4), 811–818 (2011). https://doi.org/10.1007/s11431-010-4240-9
6. Wang, T., Brivio, S., Cianci, E., Wiemer, C., Perego, M., Spiga, S., Lanza, M.: Improving HfO_2-based resistive switching devices by inserting a TaO_x thin film via engineered in situ oxidation. ACS Appl. Mater. Interfaces **14**(21), 24565–24574 (2022). https://doi.org/10.1021/acsami.2c03364
7. Stathopoulos, S., Khiat, A., Trapatseli, M., Cortese, S., Serb, A., Valov, I., Prodromakis, T.: Multibit memory operation of metal-oxide bi-layer memristors. Sci. Rep. **7**(1), 17532 (2017). https://doi.org/10.1038/s41598-017-17785-1
8. Yao, P., Wu, H., Gao, B., Eryilmaz, S.B., Huang, X., Zhang, W., Zhang, Q., Deng, N., Shi, L., Wong, H.-S.P., Qian, H.: Face classification using electronic synapses. Nat. Commun. **8**(1), 15199 (2017). https://doi.org/10.1038/ncomms15199
9. Yoon, J.H., Song, S.J., Yoo, I.-H., Seok, J.Y., Yoon, K.J., Kwon, D.E., Park, T.H., Hwang, C.S.: Highly uniform, electroforming-free, and self-rectifying resistive memory in the $Pt/Ta_2O_5/HfO_{2-x}$/TiN structure. Adv. Funct. Mater. **24**, 5086–5095 (2014). https://doi.org/10.1002/adfm.201400064
10. Park, M.R., Abbas, Y., Abbas, H., Hu, Q., Lee, T.S., Choi, Y.J., Yoon, T.-S., Lee, H.-H., Kang, C.J.: Resistive switching characteristics in hafnium oxide, tantalum oxide and bilayer devices. Microelectron. Eng. **159**, 190–197 (2016). https://doi.org/10.1016/j.mee.2016.03.043
11. Yoon, J.H., Yoo, S., Song, S.J., Yoon, K.J., Kwon, D.E., Kwon, Y.J., Park, T.H., Kim, H.J., Shao, X.L., Kim, Y., Hwang, C.S.: Uniform self-rectifying resistive switching behavior via preformed conducting paths in a vertical-type Ta_2O_5/HfO_2-x structure with a sub-μ m2 cell area. ACS Appl. Mater. Interfaces. **8**(28), 18215–18221 (2016). https://doi.org/10.1021/acsami.6b05657
12. Ma, H., Zhang, X., Wu, F., Luo, Q., Gong, T., Yuan, P., Xu, X., Liu, Y., Zhao, S., Zhang, K., Lu, C., Zhang, P., Feng, J., Lv, H., Liu, M.: A self-rectifying resistive switching device based on HfO_2/TaO_x bilayer structure. IEEE Trans. Electron. Dev. **66**(2), 924–928 (2019). https://doi.org/10.1109/TED.2018.2883192
13. Ryu, J.-H., Mahata, C., Kim, S.: Long-term and short-term plasticity of ta2o5/hfo2 memristor for hardware neuromorphic application. J. Alloy. Compd. **850**, 156675 (2021). https://doi.org/10.1016/j.jallcom.2020.156675
14. Ryu, H., Kim, S.: Implementation of a reservoir computing system using the short-term effects of $Pt/HfO_2/TaO_x/TiN$ memristors with self-rectification. Chaos, Solitons Fractals **150**, 111223 (2021). https://doi.org/10.1016/j.chaos.2021.111223
15. Park, M., Jeon, B., Park, J., Kim, S.: Memristors with nociceptor characteristics using threshold switching of $Pt/HfO_2/TaO_x/TaN$ devices. Nanomaterials **12**(23) (2022). https://doi.org/10.3390/nano12234206
16. Luo, Q., Xu, X., Liu, H., Lv, H., Gong, T., Long, S., Liu, Q., Sun, H., Banerjee, W., Li, L., Gao, J., Lu, N., Liu, M.: Super nonlinear RRAM with ultra-low power for 3D vertical nano-crossbar arrays. Nanoscale **8**, 15629–15636 (2016). https://doi.org/10.1039/C6NR02029A
17. Kim, W., Rösgen, B., Breuer, T., Menzel, S., Wouters, D., Waser, R., Rana, V.: Nonlinearity analysis of TaOx redox-based RRAM. Microelectron. Eng. **154**, 38–41 (2016). https://doi.org/10.1016/j.mee.2016.01.025
18. Applied Materials Inc.: Apparatuses for atomic layer deposition. US Patent US8343279B2 (2004)
19. Micron Technology Inc.: Atomic layer deposited hafnium tantalum oxide dielectrics. U.S. Patent US7560395B2 (2005)
20. Niu, G., Kim, H.-D., Roelofs, R., Perez, E., Schubert, M.A., Zaumseil, P., Costina, I., Wenger, C.: Material insights of HfO_2-based integrated 1-transistor-1-resistor resistive random access memory devices processed by batch atomic layer deposition. Sci. Rep. **6**(1), 28155 (2016). https://doi.org/10.1038/srep28155
21. Grossi, A., Perez, E., Zambelli, C., Olivo, P., Miranda, E., Roelofs, R., Woodruff, J., Raisanen, P., Li, W., Givens, M., Costina, I., Schubert, M.A., Wenger, C.: Impact of the precursor chemistry and process conditions on the cell-to-cell variability in 1T–1R

based HfO_2 RRAM devices. Sci. Rep. **8**(1), 11160 (2018). https://doi.org/10.1038/s41598-018-29548-7
22. Blaschke, D., Munnik, F., Grenzer, J., Rebohle, L., Schmidt, H., Zahn, P., Gemming, S.: A correlation study of layer growth rate, thickness uniformity, stoichiometry, and hydrogen impurity level in HfO2 thin films grown by ALD between 100°c and 350°c. Appl. Surf. Sci. **506**, 144188 (2020). https://doi.org/10.1016/j.apsusc.2019.144188
23. McIntyre, P.: Bulk and interfacial oxygen defects in HfO2 gate dielectric stacks: a critical assessment. ECS Trans. **11**(4), 235–249 (2007). https://doi.org/10.1149/1.2779564
24. Traoré, B., Blaise, P., Vianello, E., Perniola, L., De Salvo, B., Nishi, Y.: HfO2-based RRAM: electrode effects, Ti/HfO2 interface, charge injection, and oxygen (o) defects diffusion through experiment and ab initio calculations. IEEE Trans. Electron Dev. **63**(1), 360–368 (2016). https://doi.org/10.1109/TED.2015.2503145
25. Kunwar, S., Somodi, C.B., Lalk, R.A., Rutherford, B.X., Corey, Z., Roy, P., Zhang, D., Hellenbrand, M., Xiao, M., MacManus-Driscoll, J.L., Jia, Q., Wang, H., Joshua Yang, J., Nie, W., Chen, A.: Protons: critical species for resistive switching in interface-type memristors. Adv. Electron. Mater. **9**(1), 2200816. https://doi.org/10.1002/aelm.202200816
26. Chiu, F.-C.: A review on conduction mechanisms in dielectric films. Adv. Mater. Sci. Eng. **2014**, 578168 (2014). https://doi.org/10.1155/2014/578168
27. Flannery, W.E., Pollack, S.R.: Electron transfer processes through tantalum–tantalum-oxide diodes. J. Appl. Phys. **37**(12), 4417–4422 (1966). https://doi.org/10.1063/1.1708052
28. Wittmer, M., Noser, J., Melchior, H.: Oxidation kinetics of tin thin films. J. Appl. Phys. **52**(11), 6659–6664 (1981). https://doi.org/10.1063/1.328659
29. Dean, J.A.: Lange's Handbook of Chemistry, 15th edn. McGraw-Hill, New York (1999)
30. Pantisano, L., Afanas'ev, V.V., Cimino, S., Adelmann, C., Goux, L., Chen, Y.Y., Kittl, J.A., Wouters, D., Jurczak, M.: Towards barrier height modulation in HfO2/TiN by oxygen scavenging—dielectric defects or metal induced gap states? Microelectron. Eng. **88**(7), 1251–1254 (2011). https://doi.org/10.1016/j.mee.2011.03.057. Proceedings of the 17th Biennial International Insulating Films on Semiconductor Conference
31. Michalas, L., Stathopoulos, S., Khiat, A., Prodromakis, T.: Conduction mechanisms at distinct resistive levels of Pt/TiO2-x/Pt memristors. Appl. Phys. Lett. **113**(14), 143503 (2018). https://doi.org/10.1063/1.5040936
32. Huang, C.-H., Huang, J.-S., Lai, C.-C., Huang, H.-W., Lin, S.-J., Chueh, Y.-L.: Manipulated transformation of filamentary and homogeneous resistive switching on ZnO thin film memristor with controllable multistate. ACS Appl. Mater. Interfaces. **5**(13), 6017–6023 (2013). https://doi.org/10.1021/am4007287
33. Park, J., Kim, T.-H., Kwon, O., Ismail, M., Mahata, C., Kim, Y., Kim, S., Kim, S.: Implementation of convolutional neural network and 8-bit reservoir computing in CMOS compatible VRRAM. Nano Energy **104**, 107886 (2022). https://doi.org/10.1016/j.nanoen.2022.107886
34. John, R.A., Demirağ, Y., Shynkarenko, Y., Berezovska, Y., Ohannessian, N., Payvand, M., Zeng, P., Bodnarchuk, M.I., Krumeich, F., Kara, G., Shorubalko, I., Nair, M.V., Cooke, G.A., Lippert, T., Indiveri, G., Kovalenko, M.V.: Reconfigurable halide perovskite nanocrystal memristors for neuromorphic computing. Nat. Commun. **13**(1), 2074 (2022). https://doi.org/10.1038/s41467-022-29727-1
35. Tamanna, N., Misha, S.H., Prakash, A., Lee, D., Woo, J., Cha, E., Attarimashalkoubeh, B., Song, J., Lee, S., Moon, K., Hwang, H.: Non-linear I–V characteristics of TIOY film by optimizing thickness and trap density for selector-less RERAM. ECS Solid State Lett. **3**(10), 117 (2014). https://doi.org/10.1149/2.0021410ssl
36. Chen, Y.-C., Huang, H.-C., Lin, C.-Y., Hu, S.-T., Lin, C.-C., Lee, J.C.: Selectorless resistive switching memory: non-uniform dielectric architecture and seasoning effect for low power array applications. AIP Adv. **9**(7), 075119 (2019). https://doi.org/10.1063/1.5097233
37. Park, S.-G., Yang, M.K., Ju, H., Seong, D.-J., Lee, J.M., Kim, E., Jung, S., Zhang, L., Shin, Y.C., Baek, I.-G., Choi, J., Kang, H.-K., Chung, C.: A non-linear ReRAM cell with sub-1μ; a ultralow operating current for high density vertical resistive memory (VRRAM). In: 2012 International Electron Devices Meeting, pp. 20–812084. IEEE (2012). https://doi.org/10.1109/IEDM.2012.6479084. http://ieeexplore.ieee.org/document/6479084/
38. Aluguri, R., Kumar, D., Simanjuntak, F.M., Tseng, T.-Y.: One bipolar transistor selector—one resistive random access memory device for cross bar memory array. AIP Adv. **7**(9), 095118 (2017). https://doi.org/10.1063/1.4994948
39. Yong, Z., Persson, K.-M., Saketh Ram, M., D'Acunto, G., Liu, Y., Benter, S., Pan, J., Li, Z., Borg, M., Mikkelsen, A., Wernersson, L.-E., Timm, R.: Tuning oxygen vacancies and resistive switching properties in ultra-thin HfO_2 RRAM via TiN bottom electrode and interface engineering. Appl. Surf. Sci. **551**, 149386 (2021). https://doi.org/10.1016/j.apsusc.2021.149386
40. Egorov, K.V., Lebedinskii, Y.Y., Markeev, A.M., Orlov, O.M.: Full ALD Ta2O5-based stacks for resistive random access memory grown with in vacuo XPS monitoring. Appl. Surf. Sci. **356**, 454–459 (2015). https://doi.org/10.1016/j.apsusc.2015.07.217
41. Ma, Y., Cullen, D.A., Goodwill, J.M., Xu, Q., More, K.L., Skowronski, M.: Exchange of ions across the TiN/TaOx interface during electroformation of TaOx-based resistive switching devices. ACS Appl. Mater. Interfaces. **12**(24), 27378–27385 (2020). https://doi.org/10.1021/acsami.0c06960
42. Jeon, H., Park, J., Jang, W., Kim, H., Kang, C., Song, H., Seo, H., Jeon, H.: Resistive switching of a TaOx/TaON double layer via ionic control of carrier tunneling. Appl. Phys. Lett. **104**(15), 151603 (2014). https://doi.org/10.1063/1.4871692
43. Sugawara, T., Oshima, Y., Sreenivasan, R., McIntyre, P.C.: Electrical properties of germanium/metal-oxide gate stacks with atomic layer deposition grown hafnium-dioxide and plasma-synthesized interface layers. Appl. Phys. Lett. **90**(11), 112912 (2007). https://doi.org/10.1063/1.2472197